# Crystallographic analysis of orientational domain variants and charge-ordered domains in $La_{0.33}Ca_{0.67}MnO_3$

Renhui Wang and Jianian Gui
*Department of Applied Science, Brookhaven National Laboratory, Upton, New York 11973*
*and Department of Physics, Wuhan University, Wuhan 430072, China*

Yimei Zhu* and A. R. Moodenbaugh
*Department of Applied Science, Brookhaven National Laboratory, Upton, New York 11973*
(Received 11 July 2000; published 20 March 2001)

We present a study on the origin of twinning and antiphase domains and their relationship to charge ordering in $La_{0.33}Ca_{0.67}MnO_3$. The evolution of these orientational and charge-ordered domains is attributed to the reduction of the crystal symmetry due to the cubic to orthorhombic and, at the charge ordering temperature $T_c$, to low-temperature orthorhombic (LTO) phase transformations. The process was predicted by group theory analysis and observed with transmission electron microscopy. In both orthorhombic phases the orientation domain has six variants with 15 possible domain boundaries which can be classified as two types of reflection twins, the $90°/m\{100\}$ and the $120°/m\{110\}$ twins. Two kinds of antiphase domains and their domain interfaces, associated with the loss of translation symmetry, with lattice shifts of $a_{co}/3$ and $a_{co}/2$ also were predicted and observed for the LTO phase. This work suggests that the twin domains, which occur well above $T_c$, are not caused by charge ordering. However, the antiphase domains, which can account for the observed small $\mathbf{c}_O$ component of the incommensurate modulation at low temperature, are directly related to charge and orbital ordering in $La_{0.33}Ca_{0.67}MnO_3$. Our study clarifies the widespread misunderstanding of twinning being equivalent to charge ordering in the system.

DOI: 10.1103/PhysRevB.63.144106 PACS number(s): 68.37.Lp, 61.72.Mm

## I. INTRODUCTION

The fascinating physical properties of $La_{1-x}Ca_xMnO_3$ perovskite oxides, including their colossal magnetoresistance and the associated rich fundamental physics, have been extensively explored[1–8] in recent years. The perovskite oxides display structural transitions at various temperatures and doping levels, and exhibit intriguing paramagnetic, ferromagnetic, and antiferromagnetic behaviors that can be attributed to the interplay between charge ordering, orbital ordering, and magnetic ordering. Compared with other exotic oxides, such as nickelates and cuprate superconductors, the lattice displacement due to the Jahn-Teller distortion induced by charge and orbital ordering is much larger for the manganites; thus, they are ideal for understanding charge and orbital ordering behavior through the study of their crystal structures. Knowledge about the structure-properties relationship in $La_{1-x}Ca_xMnO_3$ may open the door for understanding charge ordering and stripe phases, and thus, the mechanism for superconductivity in high-temperature superconductors.

Crystals of bulk $La_{0.33}Ca_{0.67}MnO_3$ have an orthorhombic *Pnma* symmetry with lattice parameters[1] $a_O = 0.53812$ nm, $b_O = 0.75687$ nm, and $c_O = 0.53864$ nm at room temperature (RT). The lattice parameters of this room-temperature orthorhombic (RTO) phase are related to the prototypical primitive cubic perovskite as $|\mathbf{a}_O| = \sqrt{2}|\mathbf{a}_P|$, $|\mathbf{b}_O| = 2|\mathbf{a}_P|$, and $|\mathbf{c}_O| = \sqrt{2}|\mathbf{a}_P|$, where the subscripts *O* and *P* denote the orthorhombic and primitive cubic phase, respectively. The RTO phase may be transformed from a high-temperature cubic (HTC) perovskite with a space group of $Pm\bar{3}m$. Below $T_{CO} \approx 260$ K, the RTO phase transforms into a charge-ordered low-temperature orthorhombic (LTO) phase of the same space group *Pnma*, but with a tripled unit cell ($a_{CO} \approx 3a_O$, $b_{CO} = b_O$, and $c_{CO} = c_O$, the subscript CO denotes a charge-ordered state).

Several issues associated with the detailed crystal structures' symmetry, and charge and orbital ordering in $La_{0.33}Ca_{0.67}MnO_3$ are currently under debate. Contradictory experimental results and interpretations exist, based on electron, neutron, and synchrotron x-ray observations. For example, conflicting structural models, the bistripe model[8] and the Wigner-crystal model,[1–3] have been proposed. Another issue is related to domain structure, its origin and relation to charge and orbital ordering. Since the domains exist on a submicron scale, transmission electron microscopy (TEM) is uniquely suited to study such localized structure. In the literature, the twin domains observed in TEM at low temperatures have been characterized as charge-ordered domains with a wave vector running parallel to both $\mathbf{a}_O$ and $\mathbf{c}_O$ axes.[3–5] This is inconsistent with x-ray and neutron experiments.[1,7]

To address the structural model issue, we recently conducted low-temperature studies on charge and orbital ordering using quantitative energy-filtered electron-diffraction and high-resolution imaging, incorporating charge in image simulation.[9] Our observations are inconsistent with the bistripe model, because the crystal symmetry, the localized displacement and the large difference in $Mn^{3+}$ and $Mn^{4+}$ stripe spacing proposed by the model do not agree with our quantitative electron diffraction, imaging and crystal symmetry analyses.[9] Although our study supports the Wigner-crystal

 

model, detailed analysis suggests that there is additional incommensurate charge modulation in many areas with an averaged modulation wave vector of $\mathbf{q}=(0.284,0,\xi)$ with $|\xi|=0.010$ The small component $\xi$ along the $c$ axis was not observed by high-resolution x-ray or neutron diffraction. Our high resolution electron microscopic imaging revealed that the incommensurate modulation of $\mathbf{a}_{CO}=3.54\mathbf{a}_O$ consists of mixed $\mathbf{a}_{CO}=3\mathbf{a}_O$ and $\mathbf{a}_{CO}=4\mathbf{a}_O$ modulations. However, the physical origin of the small component $\xi$ along the $\mathbf{c}_O$ axis is not fully elucidated.

In this article, we report our results on the origin of twinning and its relation with charge ordering. We also address the cause of the small $\xi$ component of the charge modulation. We note that in a *Pnma* orthorhombic perovskite, there may be several types of structural domains formed during a displacive phase transition from high-temperature $Pm\bar{3}m$ cubic perovskite. Thus, we conducted a systematic group-theory analysis and *in situ* TEM experiments on the HTC-to-RTO phase transition. We not only predicted the twinning which originates from the lowering of the crystal symmetry due to the phase transitions in the system, but also experimentally witnessed all possible orientational twinning variants predicted by the group theory. From our experimental and theoretical work we conclude that charge-modulation only occurs along the $\mathbf{a}_O$ axis and is not the origin of the twin-related domains. Domains that originate from charge and orbital ordering, are antiphase domains as a result of the loss of translation symmetry caused by the tripling of the $\mathbf{a}_O$ axis during the RTO-LTO transition. The origin of the $\mathbf{c}_O$ component $\xi$ is due to the existence of the charge-ordered antiphase domains.

## II. GROUP-THEORY ANALYSIS

### A. Symmetry degeneracy and domain variants

A fundamental approach to understanding crystal structure and the possible orientation variants formed during a phase transition due to the symmetry change is to use group theory.[10–14] In the case of the HTC to RTO displacive transition in $La_{0.33}Ca_{0.67}MnO_3$, the crystal symmetry of the perovskite changes from $Pm\bar{3}m$ to *Pnma*, with the loss of both translation elements and point symmetry elements. Based on Hermann's theorem,[11,14,15] such a loss of symmetry results in an intermediate space group $Z$ which contains the space group *Pnma* as a $k$ subgroup (*klassengleiche* subgroup); at the same time it is also a $t$ subgroup (*translationengleiche* subgroup) of the space group $Pm\bar{3}m$. By analyzing the group-subgroup relations, we found the intermediate space group $Z$ to be *Cmmm*, and the maximal subgroup chain from $Pm\bar{3}m$ to *Pnma* can be expressed as

$$Pm\bar{3}m\supset[3]P4/mmm\supset[2]Cmmm \supset[2]Cmcm(\mathbf{c}'=2\mathbf{c})\supset[2]Pbnm(Pnma). \quad (1)$$

Here, the number in brackets denotes the order of each subgroup in its supergroup. $(\mathbf{c}'=2\mathbf{c})$ indicates the relationship of the basis vector $\mathbf{c}'$ of the space group *Cmcm* to the basis vector $\mathbf{c}$ of its supergroup *Cmmm*, and (*Pnma*) is the conventional short Hermann-Mauguin symbol of the space group *Pbnm*.[15]

The coset decompositions of each supergroup with respect to its subgroup in Eq. (1) are as follows:

$$Pm\bar{3}m=\{I\oplus 3^+[111]\oplus 3^-[111]\}P4/mmm, \quad (2)$$

$$P4/mmm=\{I\oplus 4^+[001]\}Cmmm, \quad (3)$$

$$Cmmm=\{I\oplus \mathbf{t}(0,0,\tfrac{1}{2})\}Cmcm, \quad (4)$$

$$Cmcm=\{I\oplus \mathbf{t}(\tfrac{1}{2},\tfrac{1}{2},0)\}Pbnm, \quad (5)$$

where $I$ is the identity operation, $\oplus$ is addition of two operations, $3^+[111]$ and $3^-[111]$ designate point symmetry operations with $+2\pi/3$ and $-2\pi/3$ rotations, respectively, around the $[111]$ axis. $\mathbf{t}(0,0,\frac{1}{2})$ is a translation operation with respect to the basis vectors of the space group *Cmcm* and $\mathbf{t}(\frac{1}{2},\frac{1}{2},0)$ a translation operation with respect to the *Pbnm*. Among these four decompositions, Eqs. (2) and (3) describe the $t$ subgroup relations, i.e., the related subgroup which loses point symmetry but retains all the translation operations, while Eqs. (4) and (5) describe the $\mathbf{k}$ subgroup relations in which some translation operations are also lost. By combining Eqs. (2) and (3) we obtain the coset decomposition of the space group $Pm\bar{3}m$ with respect to its $\mathbf{t}$ subgroup *Cmmm*:

$$Pm\bar{3}m=\{I\oplus 4^+[001]\oplus 3^-[111]\oplus 4^-[100]\oplus 3^+[111] \oplus 2[101]\}Cmmm. \quad (6)$$

The six cosets in Eq. (6) correspond to six orientational variants $K$ ($K=A$, $A'$, $B$, $B'$, $C$, and $C'$) for both the RTO′ and the LTO-orthorhomic *Pnma* perovskite. The geometric relation between orientational variants and their prototypic cubic perovskite are shown in the $[001]_P$ projection of a stereographic diagram, Fig. 1(a), where the subscript $P$ denotes the primitive cubic perovskite indexing, $\mathbf{a}_K$, $\mathbf{b}_K$, and $\mathbf{c}_K$ are the unit-cell orthogonal directions of the variant $K$, and $K/K'$ denotes the trace direction of the $K$ and $K'$ domain-boundary planes which also are schematically depicted in Figs. 1(b) and 1(c). The geometric relation between domains due to the HTC-RTO phase transition is characterized as the orthorhombic $\mathbf{b}_O$ axis being parallel to one of the equivalent $[100]_P$, $[010]_P$, and $[001]_P$ primitive cubic axes. For each $\mathbf{b}_O$ there are two additional domains generated with the interchange of $\mathbf{a}_O$ and $\mathbf{c}_O$ axes. For instance, from domain $A$ we can generate domain $A'$ with $\mathbf{a}_A=-\mathbf{b}_P+\mathbf{c}_P$, $\mathbf{b}_A=2\mathbf{a}_P$, $\mathbf{c}_A=\mathbf{b}_P+\mathbf{c}_P$; $\mathbf{a}_{A'}=\mathbf{b}_P+\mathbf{c}_P$, $\mathbf{b}_{A'}=2\mathbf{a}_P$, $\mathbf{c}_{A'}=\mathbf{b}_P-\mathbf{c}_P$. Mathematically, the basis vectors $\mathbf{a}_K$, $\mathbf{b}_K$, and $\mathbf{c}_K$ of the six variants $K$ can be related to those of $\mathbf{a}_P$, $\mathbf{b}_P$, and $\mathbf{c}_P$ of the cubic perovskite by

$$\begin{bmatrix} a_K \\ b_K \\ c_K \end{bmatrix} = M_K \begin{bmatrix} a_P \\ b_P \\ c_P \end{bmatrix},$$

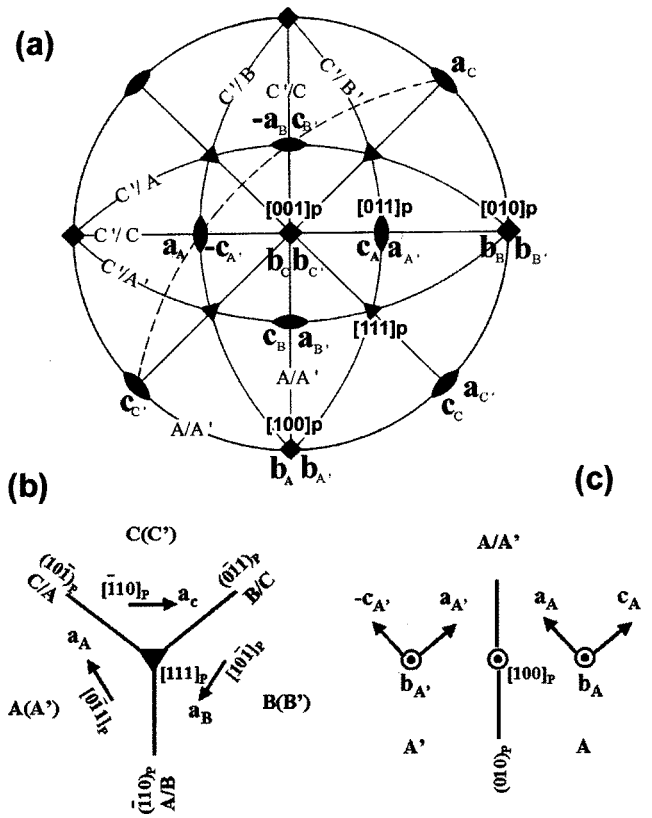


FIG. 1. Crystallographic relationship of the six orthorhombic orientation-domains $A$, $A'$, $B$, $B'$, $C$, and $C'$ and their boundaries with respect to the parent cubic-perovskite phase. (a) $[001]_P$ stereographic projection diagram. All indices with the subscript $P$ are for the primitive cubic perovskite. $\mathbf{a}_K$, $\mathbf{b}_K$, and $\mathbf{c}_K$ are basis vectors of the variant $K$ ($K=C'$, $C$, $B'$, $B$, $A'$, or $A$). (b) Schematics showing orientation relations of 120° domains $A$, $B$, and $C$, viewed along the $[111]_P$ direction. The boundaries are $m\{110\}$ type of twin-boundaries, and the $\mathbf{a}_O$ axis of $A$, $B$, and $C$ (or the $\mathbf{c}_O$ axis of $A'$, $B'$, and $C'$) rotates 120° across the boundary. (c) Schematics showing orientation relations of 90° domains $A$ and $A'$ ($B/B'$ and $C/C'$ are equivalent), viewed along the $[100]_P$ direction, parallel to $\mathbf{b}_A$ and $\mathbf{b}_{A'}$. The boundaries are $m\{100\}$ type of twin boundaries. The crystallography of the two types of boundaries are also indicated in (a).

where $M_K$ is a transformation matrix for variant $K$ ($K=A$, $A'$, $B$, $B'$, $C$, and $C'$),

$$M_A=\begin{bmatrix}0&-1&1\\2&0&0\\0&1&1\end{bmatrix},\quad M_{A'}=\begin{bmatrix}0&1&1\\2&0&0\\0&1&-1\end{bmatrix},$$

$$M_B=\begin{bmatrix}1&0&-1\\0&2&0\\1&0&1\end{bmatrix},\quad M_{B'}=\begin{bmatrix}1&0&1\\0&2&0\\-1&0&1\end{bmatrix},$$

$$M_C=\begin{bmatrix}-1&1&0\\0&0&2\\1&1&0\end{bmatrix},\quad M_{C'}=\begin{bmatrix}1&1&0\\0&0&2\\1&-1&0\end{bmatrix}.$$

With this formulation, we can easily index the diffraction patterns for each variant and understand the relative crystallographic relations, and relationship to the parent cubic phase.

Table I lists all essential symmetry operations (excluding translation operations) in the cosets for these six variants. A complete set of operations of each coset can be obtained by multiplying the essential symmetry operations with the translation operations of the subgroup under the space group of *Cmmm*. We also note that for these six variants there are 15 possible variant boundaries ($C_6^2=6(6-1)/2!$). Among them only 5 are independent such as $C'/C$, $C'/B'$, $C'/B$, $C'/A'$, and $C'/A$, represented by the five cosets, except the space group *Cmmm* of the variant $C'$ itself, listed in Table I.

In short, the symmetry degeneracy of the HTC phase gives rise to six orientational variants ($A$, $A'$, $B$, $B'$, $C$, and $C'$) from the RTO phase in $La_{0.33}Ca_{0.67}MnO_3$. Domain $A$, or $B$, or $C$ corresponds to the orthorhombic $\mathbf{b}_O$ direction being parallel to the $\mathbf{a}_P$, or $\mathbf{b}_P$, or $\mathbf{c}_P$ direction of the cubic prototype perovskite, respectively, while the domains $A'$, $B'$, and $C'$ correspond to the interchange of their $\mathbf{a}_O$ and $\mathbf{c}_O$ axes of the $A$, $B$, and $C$ domains, respectively.

### B. The crystallography of domain boundaries

We now explore the crystallography of the possible domain boundaries in light of our symmetry analysis of these six domain-variants. Based on group theory,[14] the necessary and sufficient condition for two domain boundaries $I_{lm}$ (boundary between variants $V_l$ and $V_m$) and $I_{ln}$ (boundary between variants $V_l$ and $V_n$) to be equivalent is either (1) there is a symmetry operation in the subgroup $H$ ($H=Cmmm$ in our case) which transforms $V_m$ into $V_n$ or (2) there is a symmetry operation $h$ in the coset $V_m$ whose inverse operation $h^{-1}$ belongs to the coset $V_n$. From Table I we note that the operations in cosets $3^-[111]Cmmm$, $4^-[100]Cmmm$, $3^+[111]Cmmm$, and $2[101]Cmmm$ can be transformed from one coset to another by symmetry operations in the subgroup *Cmmm*. For example, the operation $3^-[111]$ in the coset $3^-[111]Cmmm$ is transformed into the operation $3^-[\bar{1}\,\bar{1}1]$ in the coset $4^-[100]Cmmm$ by the operation $2[001]$. The operation $3^-[\bar{1}\,\bar{1}1]$ in the coset $4^-[100]Cmmm$ itself is transformed into the operation $3^+[111]$ in the coset $3^+[111]Cmmm$ by the operation $2[110]$. And the operation $3^+[111]$ is transformed into the operation $3^+[\bar{1}\,\bar{1}1]$ in the coset $2[101]Cmmm$ by the operation $2[001]$. Here, the $2[001]$, $2[110]$, and $2[101]$ are operations of *Cmmm*. Therefore, the boundaries of $C'/B'$, $C'/B$, $C'/A'$, and $C'/A$ are equivalent, and we can label them, according to the convention suggested by Guymont *et al.*[12] and Guymont,[13] as $m(0\bar{1}1)$, $m(011)$, $m(\bar{1}01)$, and $m(101)$ twin boundaries (HTC setting), respectively. These boundaries have their twinning planes parallel to one of the $\{110\}_P$ types except $m(\bar{1}10)$ and $m(110)$. Namely, among the six $m\{110\}$ type operations, $m(\bar{1}10)$ and $m(110)$ operations should be excluded since they are symmetry operations of the *Cmmm* subgroup. This type of boundary features a $[100]_O$ or $[001]_O$ axis rotating 120° across the boundary

TABLE I. Orientational variants and the essential operations in cosets corresponding to these variants.

| Variant | Coset | Essential | Operations in coset | | |
|---|---|---|---|---|---|
| $V_{C'}$ | $Cmmm$ | $I$ | $2[\bar{1}10]$ | $2[110]$ | $2[001]$ |
| | | $\bar{1}$ | $m[\bar{1}10]$ | $m[110]$ | $m[001]$ |
| $V_C$ | $4^+[001]Cmmm$ | $4^+[001]$ | $2[100]$ | $2[010]$ | $4^-[001]$ |
| | | $\bar{4}^+[001]$ | $m[100]$ | $m[010]$ | $\bar{4}^-[001]$ |
| $V_{B'}$ | $3^-[111]Cmmm$ | $3^-[111]$ | $2[0\bar{1}\bar{1}]$ | $4^+[100]$ | $3^-[1\bar{1}\bar{1}]$ |
| | | $\bar{3}^-[111]$ | $m[0\bar{1}\bar{1}]$ | $\bar{4}^+[100]$ | $\bar{3}^-[1\bar{1}\bar{1}]$ |
| $V_B$ | $4^-[100]Cmmm$ | $4^-[100]$ | $3^-[\bar{1}1\bar{1}]$ | $3^-[\bar{1}\bar{1}1]$ | $2[011]$ |
| | | $\bar{4}^-[100]$ | $\bar{3}^-[\bar{1}1\bar{1}]$ | $\bar{3}^-[\bar{1}\bar{1}1]$ | $m[011]$ |
| $V_{A'}$ | $3^+[111]Cmmm$ | $3^+[111]$ | $2[\bar{1}0\bar{1}]$ | $4^-[010]$ | $3^+[\bar{1}1\bar{1}]$ |
| | | $\bar{3}^+[111]$ | $m[\bar{1}0\bar{1}]$ | $\bar{4}^-[010]$ | $\bar{3}^+[\bar{1}1\bar{1}]$ |
| $V_A$ | $2[101]Cmmm$ | $2[101]$ | $3^+[\bar{1}\bar{1}1]$ | $3^+[1\bar{1}\bar{1}]$ | $4^+[010]$ |
| | | $m[101]$ | $\bar{3}^+[\bar{1}\bar{1}1]$ | $\bar{3}^+[1\bar{1}\bar{1}]$ | $\bar{4}^+[010]$ |

[Fig. 1(a)]. This crystal geometry may be clearly demonstrated when observed along the cubic $[111]_P$ direction [Fig. 1(b)]. On the other hand, the coset $4^+[001]Cmmm$ corresponding to the variant $C$ cannot be transformed into other cosets by any operations in the subgroup $Cmmm$. The inverse operation of any operation in the coset still belongs to this coset, so that no other coset contains an inverse operation of the operations in the coset $4^+[001]Cmmm$. Therefore, this type of boundary, say $C'/C$, is clearly distinct from the abovementioned four $m\{110\}_P$ type of boundaries, and can be labeled as $m(100)$ or $m(010)$ twin-boundary with twinning plane of $\{100\}$. This type of boundary features a $[100]_O$ or $[001]_O$ axis rotating 90° across the boundary [Fig. 1(a)], i.e., with a parallel $\mathbf{b}_O$ axis but interchanged $\mathbf{a}_O$ and $\mathbf{c}_O$ axes of the two neighboring domains. This situation may be clearly demonstrated when observed along the cubic $[100]_P$ direction [Fig. 1(c)].

Thus, we can classify the interface between any two orientational domains in the orthorhombic $La_{0.33}Ca_{0.67}MnO_3$ into two types of twin boundaries. One is the $m\{110\}$ type. In the cubic perovskite, there are six $\{110\}$ lattice planes. Two belong to the domains $J$ and $J'$, and two belong to domains $K$ and $K'$ (Here $J$ and $J'$ or $K$ and $K'$ are assigned to $A$ and $A'$, or $B$ and $B'$, or $C$ and $C'$ described above with $J \neq K$). The remaining two $\{110\}$ planes are the domain boundaries $J/K$ (or $J'/K'$) and $J/K'$ (or $J'/K$). The second type is $m\{100\}$. There are three $\{100\}$ lattice planes in the cubic perovskite; one belongs to the domains $J$ and $J'$, and the other two are the domain boundaries $J/J'$. The above analysis is generally valid for any crystal system which is involved in transformation from the space group $Pm\bar{3}m$ to $Pnma$.

## III. OBSERVATIONS AND DISCUSSIONS

### A. Experimental

The *in situ* observations of electron diffraction and high-resolution imaging of domain variants and domain boundaries before, during, and after the phase transformations were conducted with a JEM 3000*F* field-emission transmission electron microscope (TEM) operated at 300 kV. For the heating and cooling experiments we used Gatan heating and liquid $He_2/N_2$ cooling stages with a temperature range of 15–1300 K. Most observations were recorded on film negatives; for quantitative analysis imaging plates and CCD camera were also used. TEM samples were prepared via standard processes of mechanical polishing, dimpling, and ion milling. The procedures of sample fabrication and characterization using synchrotron x-ray of polycrystalline $La_{0.33}Ca_{0.67}MnO_3$ were reported previously.[9]

### B. The HTC-RTO transition

To verify the symmetry analyses associated with the high-temperature cubic (HTC) to orthorhombic (RTO) phase transformation, we conducted *in situ* experiments by heating samples in the microscope and dynamically observing symmetry changes in diffraction pattern of the crystal. Figure 2 shows the morphology of three grains in $La_{0.33}Ca_{0.67}MnO_3$ with the left grain being viewed along the $[100]_O$ or $[011]_P$ direction. Before the sample is heated, the diffraction pattern of the grain is similar to Fig. 2(d), displaying the orthorhombic $(011)_O$ type of reflection, which is forbidden for the cubic phase. When the temperature reaches is >1073 K, the $\{011\}_O$ type of reflections disappear. Figures 2(a) and (b) are a bright-field (BF) image and a diffraction pattern of the same area, recorded at 1073 K in which the $(011)_O$ reflection is completely extinct. During cooling, the fundamental reflections of the HTC remain the same, but the superlattice reflections of the $(011)_O$ type reappear, as shown in Fig. 2(d) after a thermal cycle. Figure 2(c) is a corresponding BF image taken at RT from the same area shown in Fig. 2(a). To determine the transformation temperature for thin $La_{0.33}Ca_{0.67}MnO_3$ crystals, we examined different areas in several samples. We found that the average phase transformation temperature is about ~1073 K, which is very similar to the recent x-ray observation from powder samples.[16] The transition temperature is much higher than we anticipated from extrapolating the $a_O$-, $b_O$-, and $c_O$-lattice-parameter

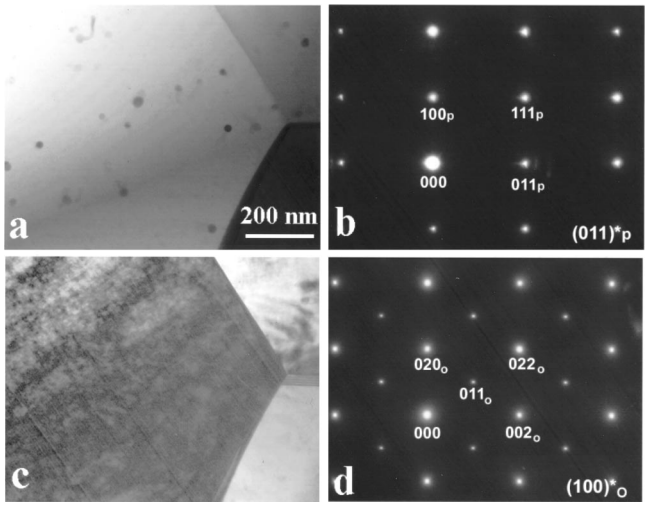


FIG. 2. *In situ* TEM observations of the cubic to orthorhombic (HTC-RTO) phase transition in $La_{0.33}Ca_{0.67}MnO_3$. (a) BF image taken at 1073 K; (b) the corresponding diffraction pattern of the $(01\bar{1})^*_P$ zone from the left grain in (a); (c)–(d) BF image and the corresponding diffraction pattern of the $(\bar{1}00)^*_O$ zone from the same area in (a) taken at room temperature showing the presence of the $(011)_O$ type of reflections.

change ($a_P = c_P$ for HTC) as a function of temperature from 160–300 K measured by synchrotron x rays in the LTO powder of $La_{0.33}Ca_{0.67}MnO_3$.[1]

### C. Distinguishing between the $a_O$ and $c_O$ axis of the RTO and LTO phases

As mentioned in the Introduction, one debate in the study of charge and orbital ordering in $La_{0.33}Ca_{0.67}MnO_3$ is whether the charge ordering occurs along the $a_O$ axis,[1] or both $a_O$ and $c_O$ axes.[3] The latter suggestion was based on TEM observations that two charge-ordered superlattices often have a 90° orientation with a twinning symmetry below $T_{CO}$. Thus, the twinning domains have been referred to as charge-ordered domains originating from charge and orbital ordering. Based on our symmetry analysis described in Sec. II, twinning may develop in the RTO phase as it transforms from the HTC phase. Since the space group *Pnma* is unchanged for the RTO and LTO phases, the charge ordering below $T_c$ does not alter the symmetry of the crystal, but induces charge modulations in the crystal structure which makes twinning readily visible in electron diffraction. Distinguishing the $a_O$ and $c_O$ axes in the RTO phase is not trivial. Since the difference in lattice parameters is less than 0.1% ($a_O = 0.53812$ nm and $c_O = 0.53864$ nm), the splitting of diffraction spots due to twinning is hardly detectable by diffraction. In conventional bright-field and dark-field (DF) imaging, such a small difference in lattice parameters yields a commensurate small difference in the excitation error between neighboring domains; thus they can be easily missed. However, we can take advantage of the different extinction rules of *Pnma* for the $(0k1)$ and the $(hk0)$ reflections to differentiate the $(100)^*_O$ and $(001)^*_O$ diffraction projection. Figure 3 is the schematics of the RTO $(001)^*_O$ and $(100)^*_O$ diffraction pattern, together with the corresponding $(011)^*_P$ pattern for the HTC phase [Fig. 3(a)], from which the $(001)^*_O$ and $(100)^*_O$ are transformed during the HTC to RTO transition. In the $(001)^*_O$ orientation [Fig. 3(b), assigned as domain variant $A$] the spots of $(-100)_A$, $(-110)_A$, and $(-120)_A$ types are forbidden owing to the reflection condition of $(h\,k\,0)$ being $h = 2n$ even when multiple scattering effect is considered. Although spots of $(010)_A$ type are not allowed due to the reflection condition of $(0k1)$ being $k+1 = 2n$, they may be generated through double diffraction. In contrast to the $(100)^*_O$ orientation [Fig. 3(c), assigned as variant $A'$], the spots of types $(010)_{A'}$, $(001)_{A'}$, $(021)_{A'}$, and $(012)_{A'}$, are not present because of the reflection condition of $(0k1)$ being $k+1 = 2n$. Thus, we can identify the $\mathbf{a}_O$ and $\mathbf{c}_O$ axis of the crystal in the diffraction pattern by tilting the sample so that the $[001]_O$ or $[100]_O$ direction is parallel to the beam direction, provided that the beam size is smaller than the domain size, i.e., under a single-domain electron-diffraction condition. Since both the $[001]_O$ and $[100]_O$ directions are transformed from a cubic $\langle 011\rangle_P$ direction, they coexist as orthogonal directions across the boundary. Figure 4 shows diffraction patterns used to determine the modulation direction of charge-ordering of an adjacent pair of $A$ and $A'$ type domains. A rectangular mesh pattern with an edge-length ratio of $2\sqrt{2}$ [Fig. 4(a)]

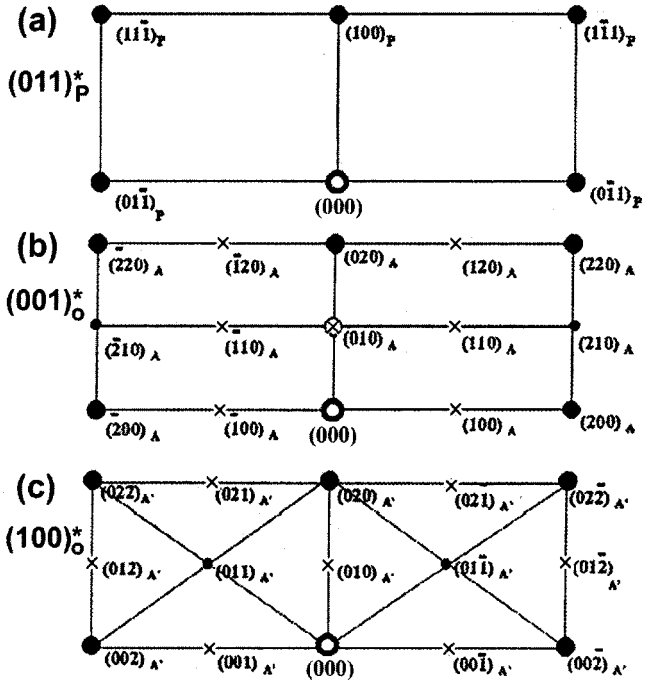


FIG. 3. Schematics of diffraction patterns showing different extinction rules of the $(001)^*_O$ and $(100)^*_O$ zone of the orthorhombic (RTO) phase, together with its parent cubic (HTC) phase in the same orientation $(011)^*_P$. (a) the $(011)^*_P$ zone of the cubic phase; (b) $(001)^*_O$; and (c) $(100)^*_O$ of the orthorhombic *Pnma* phase. The large black dots denote the primitive cubic fundamental reflections, and the small ones denote the additional reflections for the orthorhombic *Pnma* phase. The symbol $\times$ represents forbidden reflections, while $\otimes$ represents reflections that are forbidden but generated through multiple scattering.

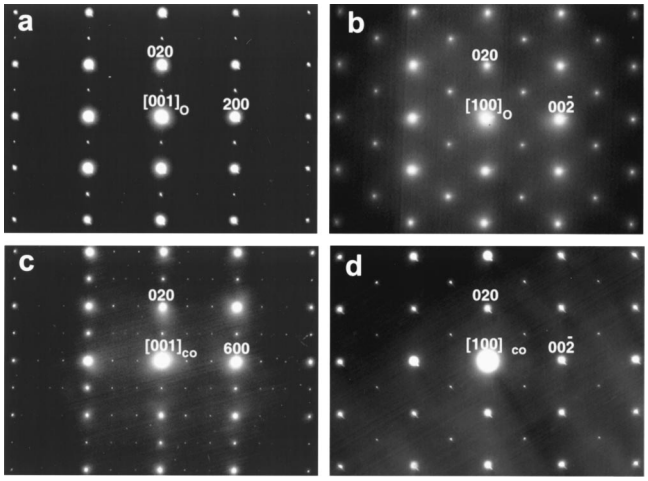


FIG. 4. *In situ* observations of orientational variant of a neighboring domain $A$ and $A'$ along the cubic $[011]_P$ axis, or the [001] and [100] axes of the orthorhombic phases, in determining the modulation direction of charge-ordering. (a) Selected area diffraction pattern from domain $A$ at RT; (b) from domain $A'$ at RT; (c) from domain $A$ at 85 K; and (d) from domain $A'$ at 85 K. Sharp, but weak, superlattice reflections of $\mathbf{q}=(\frac{2}{3}00)_O$ are clearly visible in (c).

indicates the $[001]_O$ orientation in the domain $A$. When the temperature is lowered, we observe sharp but weak superlattice reflections of a modulation wave vector $\mathbf{q}=(\frac{2}{3}00)$, Fig. 4(c). In contrast, the neighboring domain $A'$ shows a face-centered mesh at RT [Fig. 4(b)], indicating a non-$[001]_O$ orientation, or the $[100]_O$ zone axis, in the area $A'$. When temperature is lowered, no superlattice reflections were observed from domain $A'$, as shown in Fig. 4(d). Our study of two dozen cases gave the same results. These experiments reveal that charge-ordering modulation is along the $\mathbf{a}_O$, but not the $\mathbf{c}_O$, direction, the same conclusion having been made based on high-resolution synchrotron x-ray powder diffraction.[1,7] Hence the twin-related domains observed at low temperature[3–5] cannot be formed during charge ordering. In the next section we will show that these twin-related domains indeed exist in the RTO phase and originate from the HTC to RTO phase transition.

### D. Twin-related orientational domains in the RTO and LTO phases

An intriguing observation in the cubic ($Pm\bar{3}m$) to orthorhombic (*Pnma*) phase transformation in $La_{0.33}Ca_{0.67}MnO_3$ perovskite is the formation of orientational variants or twin-related domains at temperatures much higher than the charge-ordering temperature $T_{CO}$. The observation of room temperature twin-related domains is consistent with our group-theory analysis, but largely unnoticed by the scientific community. These twin-related domains become charge ordered below $T_{CO}$. The configuration and shape of the domains remain essentially the same after repeated thermal cycles. Figure 5 shows a typical example of two variants $A$ and $B$ viewed along the $[111]_P$ direction of the HTC phase

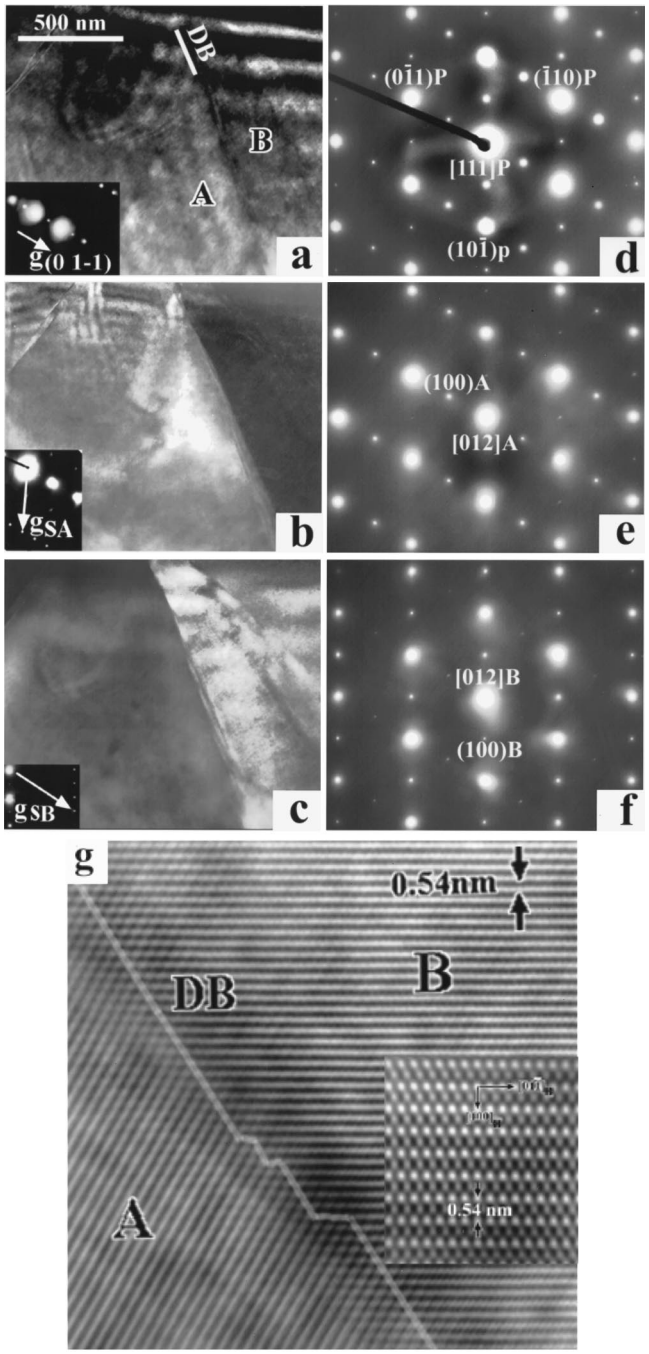


FIG. 5. Orientational domains $A$ and $B$ in orthorhombic $La_{0.33}Ca_{0.67}MnO_3$ observed at room temperature along the cubic $[111]_P$ direction. (a) BF image excited with the reflection $\mathbf{g}=(01\bar{1})_P=(\bar{2}00)_A=(12\bar{1})_B$ Note, the $A/B$ domain boundary is parallel to the $(\bar{1}10)_P$ plane. (b) DF image by selecting the reflection $\mathbf{g}_{SA}=(2\bar{1}2)_P+(01\bar{1})_P/2=(\bar{2}43)_A$ which is a superlattice reflection of domain $A$; (c) DF image by selecting $\mathbf{g}_{SB}=(30\bar{2})_P+(10\bar{1})_P/2=(36\bar{2})_B$ which is a superlattice reflection of domain $B$; (d)–(f) Selected area diffraction patterns from an area consisting of domains $A+B$ (d), $A$ (e), and $B$ (f). (g) Corresponding lattice fringe image showing the 120° rotation of the $(100)_A$ and $(100)_B$-lattice fringes across the $A$ and $B$ domain boundary. The inset is a high-resolution image from a thin region of the domain $B$ viewed along $[012]_B$.

(or the $[012]_O$ of the RTO phase). Figure 5(a) is a BF image by exciting the $(01\bar{1})_p$ fundamental reflection (RTO setting), as seen in the diffraction pattern [Fig. 5(d)], taken from both *A* and *B* domains. Figures 5(b) and (c) are DF images for domains *A* and *B* using $\mathbf{g}_{SA}=(2\bar{1}\bar{2})_P+(01\bar{1})_P/2$ and $\mathbf{g}_{SB}=(03\bar{2})_P+(10\bar{1})_P/2$, respectively, and their corresponding diffraction patterns are shown in Figs. 5(e) and 5(f) (RTO setting). The diffraction patterns display, in addition to fundamental reflections relevant to HTC, the weak spots of $(0\bar{1}\bar{1})_P/2$ types in (d), (e), and (f) which are reflections unique to the RTO phase. Note that the $(100)_A$ and the $(100)_B$ reflections of the domain *A* [Fig. 5(e)] and the domain *B* [Fig. 5(f)] are derived from the reflections of the $(0\bar{1}\bar{1})_P/2$ and the $(10\bar{1})_P/2$, respectively, of the cubic perovskite during the HTC to RTO transition. The symmetry of the diffraction patterns suggests that the domains *A* and *B* are twin related with $(\bar{1}10)_P$ as the twinning plane. From Fig. 5 we can see that the domain boundary [marked by DB in Fig. 5(a)] is parallel to the $(\bar{1}10)_P\|(\bar{1}2\bar{1})_A\|(\bar{1}2\bar{1})_B$ plane. Furthermore, the $a_O$ axis of the *A* and *B* domains rotates about 120° across the domain boundary. There are 12 such domain boundaries (*A*/*B*, *A*′/*B*′, *B*/*C*, *B*′/*C*′, *C*/*A*, *C*′/*A*′, *A*/*B*′, *A*′/*B*, *B*/*C*′, *B*′/*C*, *C*/*A*′, and *C*′/*A*) in the system, and their orientation relationship with the parent cubic phase is sketched in Fig. 1(b) when observed along the $[111]_P$ direction. The 120° rotation can be clearly seen from the $(100)_O$ lattice fringe image of the domains *A* and *B* [Fig. 5(g)] with local faceting along the boundary. The inset of Fig. 5(g) is a high-resolution image from domain *B*.

The morphology of domain boundaries *A*/*A*′, *B*/*B*′, and *C*/*C*′ are quite different from the 120° boundaries, since they are formed by the interchange of the $\mathbf{a}_O$ and $\mathbf{c}_O$ axes, with $\mathbf{b}_O$ axes of the domains remain unchanged. Figure 6 is a typical example of such an *A*/*A*′ boundary viewed along the [100] direction. Figure 6(a) is a DF image recorded at RT with the $(0\bar{1}3)_P/2=(201)_A=(10\bar{2})_{A'}$, reflection excited. The domain boundary contrast is barely visible. Figure 6(b) is the corresponding diffraction pattern of (*a*), where no twinning splitting of $(h01)_O$ diffraction spots is visible in the first-order Laue zone [Fig. 6(b)]. Twinning becomes evident when the temperature falls below $T_{CO}$ at which the charge-ordering along the $a_O$ axis occurs for the LTO phase. Figures 6(c) and (d) are the selected area diffraction patterns (RTO setting) taken from domains *A*′ and *A*, respectively, showing superlattice reflections with a modulation wave vector $\mathbf{q}\approx(h00)_O/3$, consistent with the interchange of the $a_O$ and $c_O$ axes across the $(001)_P\|(101)_A$ domain boundary. A high-resolution image of the boundary region taken at 85 K is shown in Fig. 6(e), where the 90° orthogonally orientated charge stripes with a spacing of $3a_O=1.62$ nm across the boundary are clearly visible. The fringes reveal that the domain *A* and *A*′ have a reflection-twinning geometry with the $(101)_A$ as their twinning planes, as predicted by the group-theoretical considerations described in Sec. II. The domain boundary is not sharp and may have local interpenetration of the $(100)_O$ lattice from the neighboring domains, which is quite different from the 90° twin boundary in

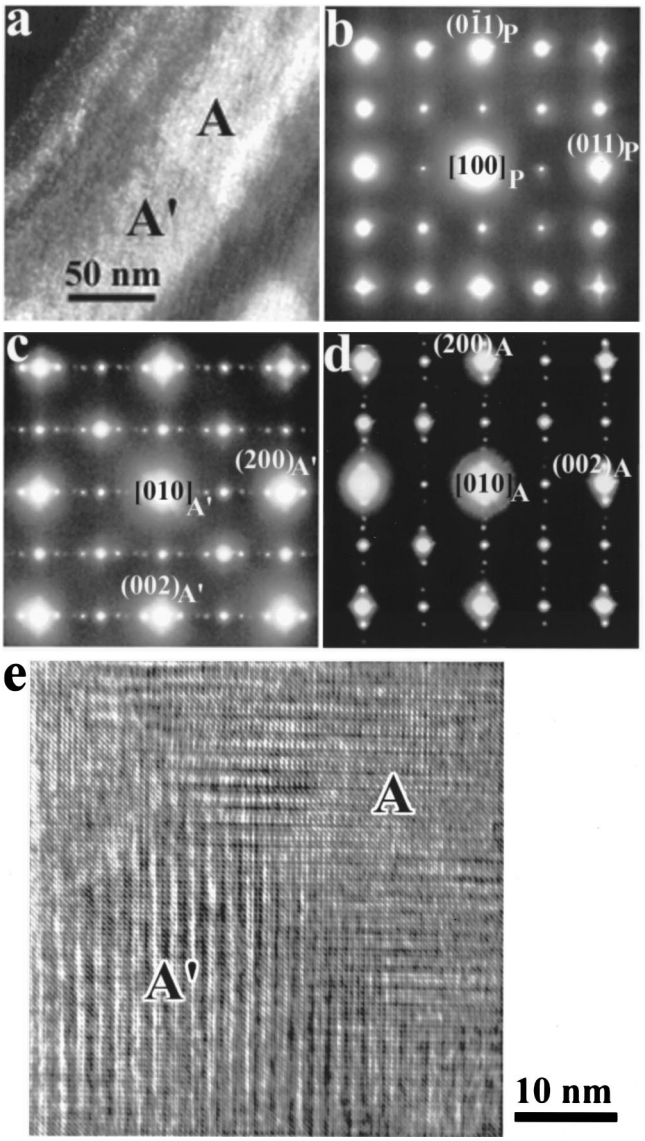


FIG. 6. Orientational domains *A* and *A*′ in orthorhombic $La_{0.33}Ca_{0.67}MnO_3$ at 300 and 85 K. (a) DF image recorded at 300 K using reflection $(201)_A=(10\bar{2})_{A'}$, (b) Corresponding diffraction at the same temperature. Note, the domain interface is parallel to the $(001)_P$ plane. (c), (d) Diffraction patterns at 85 K from the domains *A*′ and *A*, respectively, marked in (a), showing $\sim 3\mathbf{a}_O$ charge-ordering modulation in two orthogonal directions in *A*′ and *A*. (e) HREM image of the area at 85 K, showing 90° rotation of the tripled $(100)_O$ lattice fringes across the domain boundary.

$YBa_2Cu_3O_7$-$\delta$.[17] On the other hand, when domains *A* and *A*′ are observed along cubic $[011]_P$ axis, the *A*/*A*′ boundary, $(010)_P$ or $(001)_P$ plane, will be 45° inclined, as evident in Fig. 1(a), and their diffraction patterns will be along $[001]_A$ axis for domain *A* and $[100]_{A'}$ axis for *A*′ with the same $\mathbf{b}_O$ axis but interchanged $\mathbf{a}_O$ and $\mathbf{c}_O$ axes, as experimentally observed in Figs. 4(a) and 4(b), respectively.

### E. Antiphase domains and antiphase boundaries in the RTO and LTO phases

The formation of antiphase domains and domain boundaries often results from the loss of translation symmetry of a

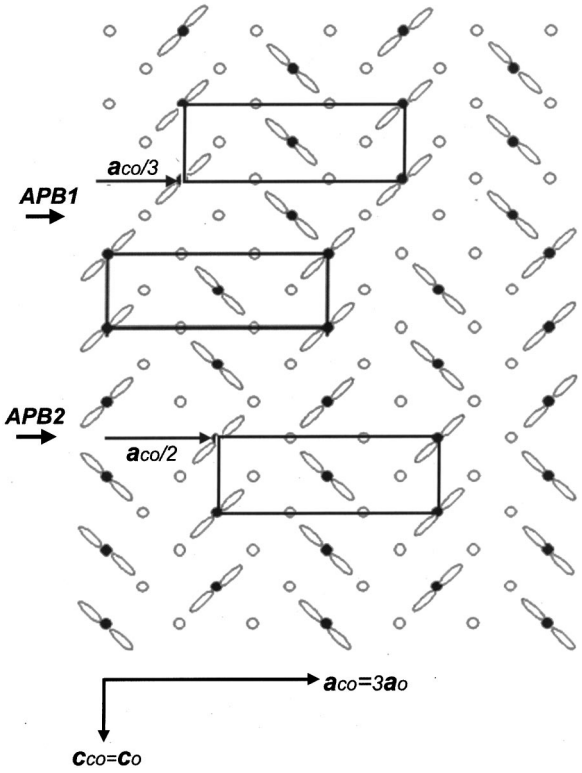


FIG. 7. Schematic drawing of atomic structures of two types of antiphase boundaries (APBs) associated with the charge and orbital ordering. The rectangular boxes indicate the unit cell projected onto the $\mathbf{a}_{CO}$-$\mathbf{c}_{CO}$ plane. $Mn^{4+}$ and $Mn^{3+}$ ions are designated, respectively, by plain circles and solid dots with orbitals. There is a lattice translation of $a_O = a_{CO}/3 = 0.54$ nm across APB1, and $a_{CO}/2 = 0.81$ nm across APB2.

crystal. In our group-theory consideration, the coset decompositions [Eqs. (4) and (5)] suggest that there may also exist antiphase domain boundaries with a lattice translation of $\mathbf{t}(0,0,\frac{1}{2})$, or $\mathbf{t}(\frac{1}{2},\frac{1}{2},0)$, or $\mathbf{t}(\frac{1}{2},\frac{1}{2},\frac{1}{2})$ (*Pbnm* setting) due to the enlarged unit cell of the RTO phase, i.e., a reduced translation symmetry compared with the HTC phase. By combining the coset decomposition Eqs. (4), (5), and (6), we can also predict the existence of translation twins in $La_{0.33}Ca_{0.67}MnO_3$. The existence of such translation-symmetry-related domains and domain boundaries in the RTO phase can be verified using high-resolution TEM, and will be discussed in a separate paper.

Here, we focus on the translation-symmetry-related domain and domain boundary of the LTO phase since it is directly associated with charge and orbital ordering, and may be of significant importance in understanding the unusual physical properties of the material. When the temperature drops below the charge order-disorder transition temperature, the crystal unit cell along the $a_O$-axis triples, leaving the crystal point symmetry unchanged. Based on our symmetry analysis, the enlargement of the unit cell along the $a_O$ axis would introduce antiphase boundaries (APBs). The most common one is the antiphase domain with a displacement of $\mathbf{R} = \pm 1/3[100]_{CO}$ (or the equivalent displacement $\mathbf{R} = \pm 2/3[100]_{CO}$) when across an APB. Another possible

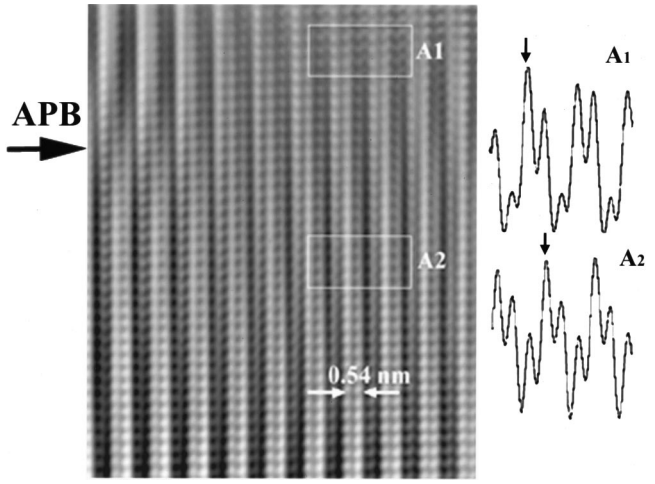


FIG. 8. High-resolution image recorded at 85 K showing two antiphase domains with a gradual lattice shift of $a_{CO}/3 = 0.54$ nm across the boundary (denoted as APB), as determined by the intensity scans of the image from the boxed areas $A1$ and $A2$. The fringe spacing corresponds to $a_O = 0.54$ nm.

translational displacement of the antiphase domain is $\mathbf{R} = \pm 1/2[100]_{OCO}$. Both structures involve symmetry broken induced by charge or orbital ordering in the crystal, as depicted in Fig. 7. For APB1 in Fig. 7, the $Mn^{4+}$ (open circles) and $Mn^{3+}$ (solid circles with orbital) sublattice has an $\mathbf{a}_O$-lattice shift across the antiphase boundary, while, for APB2, the sublattice remains the same but the orientation of the orbital ordering is reversed. Thus APB1 is essentially a charge-ordered domain boundary while APB2 is an orbital-ordered domain boundary. Note that the model for APBs in Fig. 7 established only the possible displacement vectors, not the orientations of the boundary planes, which may be parallel, or inclined, or even perpendicular to $\mathbf{a}_{CO}$.

The predicted antiphase domains and domain boundaries in the LTO phase were experimentally observed using low-temperature HRTEM. Figure 8 shows a high-resolution image of such antiphase domains recorded at 85 K with a shift of the black and white $(100)_O$ lattice fringes across the antiphase domain boundary; the superlattice contrast with a $3a_O$ periodicity is clearly visible. Line scans of the intensity of the top and bottom domains from the boxed areas $A1$ and $A2$ (averaged along the vertical direction) indicate a relative phase shift between the two with a displacement $\mathbf{R} = \frac{1}{3}[100]_{CO} \approx 0.54$ nm.

Figure 9 is another type of anti-phase domain showing $(200)_O$ lattice fringes. The white (or black) fringes running from the bottom to the top of the image change their contrast. The line scans of the two boxed areas $B_1$ and $B_2$ suggest a half unit cell lattice translation ($\mathbf{R} = \frac{1}{2}[100]_{CO} \approx 0.81$ nm) between the domains. We note that in both cases the $\mathbf{a}_O$ direction lattice shift extends a few dozen unit-cell lengths along the $\mathbf{c}_O$ axis, implying an inclined boundary or a very broad interface (marked as APB in Figs. 8 and 9) between the antiphase domains. Such broad antiphase boundaries, observed in Bi/2212 superconductors, were associated with incommensurate modulation.[18]

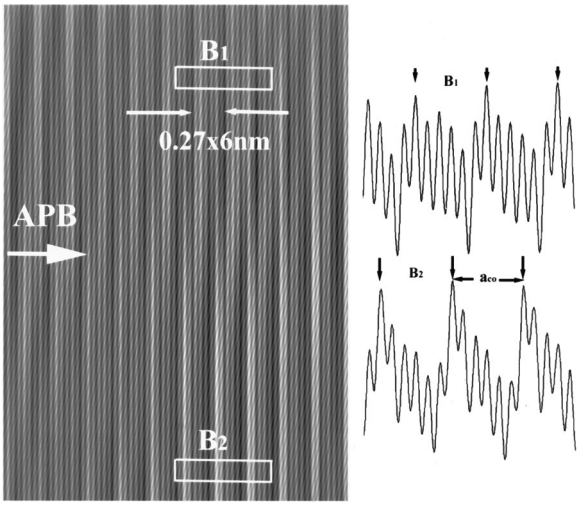


FIG. 9. High-resolution image recorded at 85 K showing two antiphase domains with a gradual lattice displacement of $a_{CO}/2 = 0.81$ nm across the boundary (denoted as APB), as determined by the intensity scans of the image from the boxed areas $B1$ and $B2$. The fringe spacing corresponds to $a_{CO}/6 = a_O/2 = 0.27$ nm.

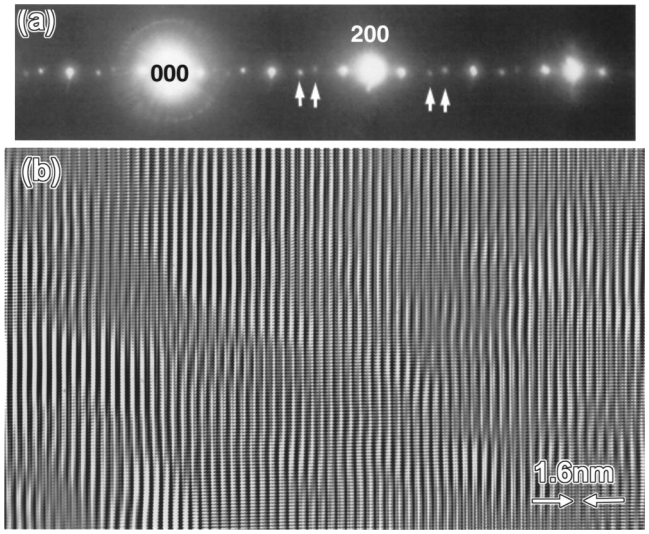


FIG. 10. (a) $(010)^*_O$ zone diffraction pattern at 85 K, revealing an incommensurate modulation with a wave vector $\mathbf{q}=(0.284,0,-0.010)$ (RTO setting). Note, the $(h00)_{CO}$ superlattice reflections do not exactly align along the $\mathbf{a}_O$ axis (as marked by the arrows), but are tilted $\sim 2°$ away from it, suggesting a small component along the $\mathbf{c}_O$ axis of the modulation wave vector. The average periodicity of the modulation is $\mathbf{a}_{CO} = 3.54\mathbf{a}_O$. (b) Lattice fringe image of a large area taken at 85 K, showing antiphase domains and wavy domain boundaries (the vertical and horizontal directions of the image are parallel to the $\mathbf{c}_O$ and $\mathbf{a}_O$ axes, respectively). The average domain size along the $[001]_O$ direction is about 16 nm.

The observation of the anti-phase domains with $\mathbf{R} = \frac{1}{3}[100]_{CO}$ may be of importance in accounting for the small $\mathbf{c}_O$-component in the incommensurate charge modulation in $La_{0.33}Ca_{0.67}MnO_3$. As clearly seen in Fig. 10(a), the superlattice reflections $\sim\frac{1}{3}(h00)_O$ (RTO setting) associated with charge ordering at low temperature are not aligned exactly along the $\mathbf{a}_O$ axis, but rather are tilted $\sim 2°$ away from the $\mathbf{a}_O$ axis. The averaged wave vector we observed was $q = (0.284,0,\xi)$ with $|\xi| = 0.010$. The breaking of symmetry due to this small component has not been previously observed by high-resolution x-ray or neutron powder diffraction, since it likely reflects the charge-ordered structure at submicrometer scale. Figure 10(b) is a lattice image of a large area in $La_{0.33}Ca_{0.67}MnO_3$ taken at 85 K with strong contrast of $3\mathbf{a}_O$ lattice fringes. Line-scan analysis, as shown in Fig. 8, indicates a displacement when across antiphase boundaries. The average dimension of antiphase domains along the $\mathbf{c}$ axis is about $10\times 3a_{CO} = 16$ nm. The shift of 0.54 nm across the boundaries and the 16 nm domain size observed in HRTEM are consistent with the $\sim 2°$ tilt $[\tan^{-1}(0.54/16) \approx 2°]$ from the $\mathbf{a}_O$ axis of the modulation wave vector observed in diffraction [Fig. 10(a)]. We note that the charge-ordered structure in $La_{0.33}Ca_{0.67}MnO_3$ is quite complex, especially the $\xi$ component. It can take either sign, and its magnitude varies with location in the sample, ranging from $-0.015 \leqslant \xi \leqslant 0.015$, depending on the area. Thus, for a relatively large area, typical dimension of $\sim 500$ $\mu$m, the contribution of the $\mathbf{c}_O$ component $\xi$ to x-ray diffraction may be averaged out to zero. This once again points out the significance of TEM in revealing the localized structure of a complex material.

## IV. CONCLUSION

In conclusion, we theoretically predicted and experimentally observed six possible domain variants ($A$, $A'$, $B$, $B'$, $C$, and $C'$) in the orthorhombic $La_{0.33}Ca_{0.67}MnO_3$ (the RTO and LTO phases) as a result of lowering in symmetry from its parent cubic perovskite (the HTC phase). There are 15 domain boundaries which can be classified into two categories, $m\{100\}$ and $m\{110\}$; both are twin related. The former is associated with neighboring domains with their $b_O$ axes parallel but $\mathbf{a}_O$ and $\mathbf{c}_O$ axes interchanged. Such 90° twin-related domains exist at temperatures far above the charge-ordering temperature $T_{CO}$. Thus, the charge-ordered domains reported in the literature[3–5] are not domains with two orthogonal modulation wave-vectors along the $\mathbf{a}_O$ and $\mathbf{c}_O$ axes. Rather they are preexisting twins, with charge-ordering developing only along the $\mathbf{a}_O$ axis (not $c_O$ axis) in each domain. On the other hand, the observed antiphase domains in HRTEM, which are associated with the charge and orbital ordering and with the tripling of the $a_O$-lattice constant, can explain the observed incommensurate charge modulation with a small $\mathbf{c}_O$ component $\xi$ in electron diffraction.

## ACKNOWLEDGMENTS

This work was supported by the Division of Materials Sciences, U.S. Department of Energy, under Contract No. DE-AC02-98CH10886. Work at Wuhan University by R.W. and J.G. was supported by the National Natural Science Foundation of China.

*Corresponding author. Email address: zhu@bnl.gov

[1] P. G. Radaelli, D. E. Cox, L. Capogna, S.-W. Cheong, and M. Marezio, Phys. Rev. B **59**, 14 440 (1999).
[2] M. T. Fernandez-Diaz, J. L. Martinez, J. M. Alonso, and E. Herrero, Phys. Rev. B **59**, 1277 (1999).
[3] C. H. Chen, S.-W. Cheong, and H. Y. Hwang, J. Appl. Phys. **81**, 4326 (1997).
[4] C. H. Chen and S.-W. Cheong, Phys. Rev. Lett. **76**, 4042 (1996).
[5] A. P. Ramirez, P. Schiffer, S.-W. Cheong, C. H. Chen, W. Bao, T. T. M. Palstra, P. L. Gammel, D. J. Bishop, and B. Zegarski, Phys. Rev. Lett. **76**, 3188 (1996).
[6] P. G. Radaelli, D. E. Cox, M. Marezio, S.-W. Cheong, P. E. Schiffer, and A. P. Ramirez, Phys. Rev. Lett. **75**, 4488 (1995).
[7] P. G. Radaelli, D. E. Cox, M. Marezio, and S.-W. Cheong, Phys. Rev. B **55**, 3015 (1997).
[8] S. Mori, C. H. Chen, and S.-W. Cheong, Nature (London) **392**, 473 (1998).
[9] Renhui Wang, Jianian Gui, Yimei Zhu, and A. R. Moodenbaugh, Phys. Rev. B **61**, 11 946 (2000).
[10] G. Van Tendeloo and S. Amelinckx, Acta Crystallogr., Sect. A: Cryst. Phys., Diffr., Theor. Gen. Crystallogr. **30**, 431 (1974).
[11] H. Wondratschek and W. Jeitschko, Acta Crystallogr., Sect. A: Cryst. Phys., Diffr., Theor. Gen. Crystallogr. **32**, 664 (1976).
[12] M. Guymont, D. Gratias, R. Portier, and M. Fayard, Phys. Status Solidi A **38**, 629 (1976).
[13] M. Guymont, Phys. Rev. B **18**, 5385 (1978).
[14] Renhui Wang and K. H. Kuo, *Symmetry Groups in Crystallography* (China Science Press, Beijing, 1990) (in Chinese).
[15] *International Tables for Crystallography*, edited by T. Hahn (Reidel, Dordrecht, 1983), Vol. A, p. 727.
[16] Jiaqing He, Renhui Wang, and Jianian Gui, Acta Phys. Sin. (to be published).
[17] Y. Zhu, M. Suenaga, J. Tafto, and D. O. Welch, Phys. Rev. B **44**, 2871 (1991).
[18] Y. Zhu and J. Tafto, Philos. Mag. A **74**, 307 (1996).